frontiers | Frontiers in Chemistry

TYPE Original Research
PUBLISHED 21 October 2022
DOI 10.3389/fchem.2022.1027024

OPEN ACCESS

EDITED BY
Suvardhan Kanchi,
Sambhram Institute of Technology, India

REVIEWED BY
Malik Khan,
Institute of Physical Chemistry (PAN), Poland
Bidhan Pandit,
Universidad Carlos III de Madrid, Spain

*CORRESPONDENCE
Mushtaq Ahmad,
mushtaq.a@comsats.edu.pk
Muhammad Azeem,
mazeem@sharjah.ac.ae

SPECIALTY SECTION
This article was submitted to Green and Sustainable Chemistry, a section of the journal Frontiers in Chemistry

RECEIVED 24 August 2022
ACCEPTED 03 October 2022
PUBLISHED 21 October 2022

CITATION
Ahmed S, Ahmad M, Yousaf MH, Haider S, Imran Z, Batool SS, Ahmad I, Shahzad MI and Azeem M (2022), Solvent-free synthesis of $NiCo_2S_4$ having the metallic nature. *Front. Chem.* 10:1027024. doi: 10.3389/fchem.2022.1027024

Solvent-free synthesis of $NiCo_2S_4$ having the metallic nature

Sardar Ahmed[1], Mushtaq Ahmad[1]*, Muhammad Hasnain Yousaf[1], Sumain Haider[1], Zahid Imran[1], S. S. Batool[1], Ishaq Ahmad[2,3], Muhammad Imran Shahzad[4] and Muhammad Azeem[5]*

[1]Catalysis and Sensing Materials Group, Department of Physics, COMSATS University Islamabad, Islamabad, Pakistan, [2]Department of Physics, The University of Hong Kong, Pokfulam, Hong Kong SAR, China, [3]Department of Chemistry, University of Sialkot, Sialkot, Pakistan, [4]Nanosciences and Technology Department (NS&TD), National Centre for Physics (NCP), Islamabad, Pakistan, [5]Department of Applied Physics and Astronomy, University of Sharjah, Sharjah, United Arab Emirates

Nickel-cobalt sulfide ($NiCo_2S_4$) is a prominent member of bimetallic transition metal sulfides. It is being widely used for a variety of applications such as electrode material, photocatalysis, and energy storage devices (like pseudo capacitors, supercapacitors, solar cells, and fuel cells) due to its better electronic conductivity, manageable morphology, and high capacitance. This work presents the one-step solventless synthesis of $NiCo_2S_4$ sheet-like nanostructures and then explores their metallic nature. Scanning electron microscopy (SEM) and transmission electron microscopic (TEM) analysis show the sheet-like grown morphology. Few nanorods are also seen. Except for a recent study (Xia et al. 2015) that shows metallic behavior, most of the reports show that $NiCo_2S_4$ is a semiconductor with claimed bandgap between 1.21 and 2.4 eV. In this study, we observe from UV-Vis and diffuse reflectance spectroscopy (DRS) that $NiCo_2S_4$ has a specific band gap value between 2.02 and 2.17 eV. However, IV characteristics in the temperature range of 300–400 K show that $NiCo_2S_4$ is a metal with a positive temperature coefficient of resistance consistent with a recent report. Furthermore, we see the ohmic conduction mechanism. The Arrhenius plot is drawn, and the activation energy is calculated to be 3.45 meV. The metallic nature is attributed to the coupling of two metal species (nickel and cobalt), which accounts for its superior conductivity and performance in a variety of essential applications.

KEYWORDS

solvent-free synthesis, solid state reaction, metallic behavior, x-rays diffraction, transmission election microscopy, current—voltage (I-V) characteristic

Introduction

$NiCo_2S_4$ has sparked a lot of attention in recent years, and it is being studied as a potential material for a variety of applications because of its fascinating characteristics. It is one of the important members of the bimetallic transition metal sulfides. Transition metal compounds have been known for unique properties, like inexpensive, pt.-like catalytic performance, large conductive, etc. (Guan et al., 2017; Chia et al., 2015; Tong

et al., 2018). Among the bimetallic compounds, the $NiCo_2S_4$ has a smaller optical energy bandgap and much better electronic conductivity than nickel cobalt oxides and hydroxides counterparts (Chen et al. 2013; Zhang et al., 2014). The $NiCo_2S_4$ recently achieved remarkable performance in energy storage devices like electrode material in supercapacitors (Zhu et al. 2015; Gao and Huang, 2017; Zheng et al., 2018), catalysis (Zhang et al., 2014; Wu et al., 2018; Wang et al., 2019), and dye-sensitized solar cell (Lin and Chou, 2013; Yang et al., 2014). Most studies on $NiCo_2S_4$, like other chalcogenides, establish that it is semiconducting, with a claimed bandgap between 1.2 and 2.4 eV (Chen et al. 2013; Du et al., 2014; Sarawutanukul et al., 2020). However, a very recent study (Xia et al., 2015) has proven that this material is behaving like a metal, based on optical and electrical results. They have reported that at room temperature the resistivity of $NiCo_2S_4$ nanostructures is around 10^3 μΩ cm, which then decreases with the decrease in temperature. It denotes a positive temperature coefficient of resistance, indicating the conducting nature of the $NiCo_2S_4$ nanostructures. Moreover, it is important to mention the effects of cations distributions in the bimetallic sulfides because the variation in cations influences the electroactive nature of the material for energy generation. Although, the substitution of cobalt with nickel and *vice versa* does not change the crystal structure of the compound (Chen et al., 2013), but cobalt-rich presence as compared to nickel adds more holes (*p*-type) i.e., makes less conductive material and when there is more presence of nickel, the material gets more electrons (*n*-type) hence causes more conduction (Gervas et al., 2018). The replacement of Ni^{2+} ions with Co^{2+} ions in ferrite materials though increases the magnetic parameters such as coercivity (Patil et al., 2022). UV-Vis spectra reported by Hu et al. (2012) showed nearly a straight line which revealed that there is no absorption during the measurement hence no optical bandgap. So, the behavior of this material remains debatable. Being motivated by these analyses we also aimed to know the behavior.

Previously, $NiCo_2S_4$ nanostructures have been synthesized using a variety of well-known methods such as hydrothermal (Chen et al., 2013; Yu and Lin, 2016; Wei et al., 2017), solvothermal (Xin et al., 2020), electrodeposition (Chen et al., 2014; Cui et al., 2022), co-precipitation (Wang et al., 2016; Nan et al., 2018), etc. There is always a challenge to synthesize bimetallic compounds with desired morphology under relatively simpler conditions. Solventless thermolysis of elemental xanthates complexes are processed recently to prepare $NiCo_2S_4$ nanostructures (Khan et al., 2018; Shombe et al., 2021; Shombe et al., 2022). In this research work, we have successfully synthesized $NiCo_2S_4$ nanostructures using quite a simple, one-step, and inexpensive solvent-free (solid-state reaction route). We have studied the crystalline structure, built-in morphology, and a detailed understanding of its optical and electrical properties to determine the origin of this material and its extraordinary performance for various applications.

Experimental details

For the synthesis of $NiCo_2S_4$, nickel acetate tetrahydrate ($C_4H_6NiO_4$). $4H_2O$, cobalt acetate tetrahydrate ($C_4H_6CoO_4$). $4H_2O$, and thiourea $SC(NH_2)_2$ were purchased from Sigma Aldrich and were of analytical grade, so used without any further purification. The stoichiometric amounts of these three precursors were mixed and ground in a pestle and mortar for 40 min to get a homogeneous mixture. In addition, we used a few drops of ethanol throughout the grinding process to improve the powder's mixing. After that, the uniform mixture was put into the crucible for heat treatment. In a sequence, we have taken three random temperatures of 200°C, 300°C, and 400°C for the same reaction time (7 h). The possible chemical reactions during $NiCo_2S_4$ formation are suggested as follows.

Firstly, thiourea decomposes at a temperature of about 150°C (Ahmad et al., 2013a; Ahmad et al., 2013b; Ahmad et al., 2013c), as shown in the equation below.

$$SC(NH_2)_2 \xrightarrow{\sim 150^\circ C} NH_2CN + H_2S. \quad (1)$$

Then H_2S reacts with nickel acetate tetrahydrate and cobalt acetate tetrahydrate forming $NiCo_2S_4$ with a few gases that are evaporated as byproducts during the reaction.

$$2[(C_4H_6CoO_4).4H_2O] + (C_4H_6NiO_4).4H_2O + 4H_2S \rightarrow N_iCo_2S_4 + 25H_2 + 12CO_2. \quad (2)$$

The steps involved in the material's formation such as nucleation, growth, and oriented attachment are shown in Figure 1.

The powder sample prepared at 400°C was compacted into a 13 mm pellet using a hydraulic press machine at 1,200 Psi pressure for 10 min to study its electrical properties. The pellet was then sintered in an oven a 150°C for 2 h to make the material more compact. After that, we used the silver paste on both sides of the pellet to make an electrical contact.

The crystallographic structure of $NiCo_2S_4$ was studied by the x-rays diffraction (XRD) technique. The other structural parameter like crystallite size, lattice constants, texture coefficient, etc. were calculated from XRD data. The built-up surface morphology of the $NiCo_2S_4$ compound was analyzed using SEM and TEM respectively. The optical characteristics were investigated through UV-Vis. spectroscopy and DRS spectroscopy. The electrical properties of the prepared nanostructures at different temperatures were carried out through IV spectroscopy using the two-probe method.

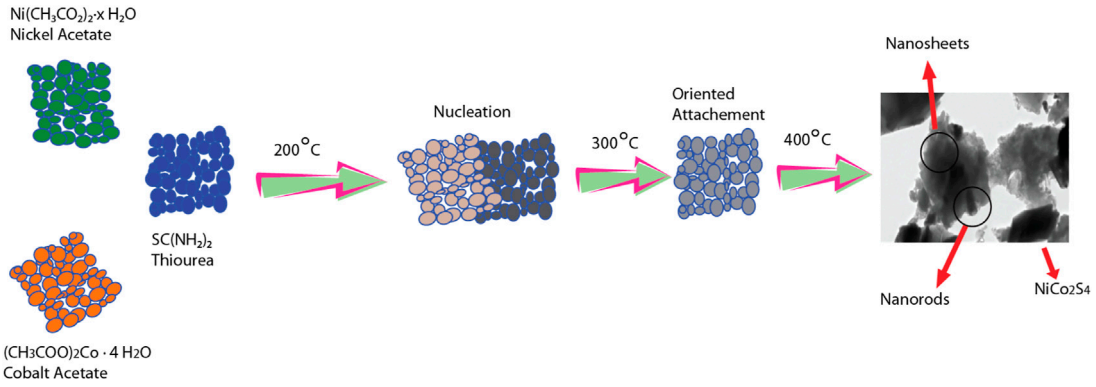

FIGURE 1
Schematic representation of steps involved e.g., nucleation, growth, and oriented attachment.

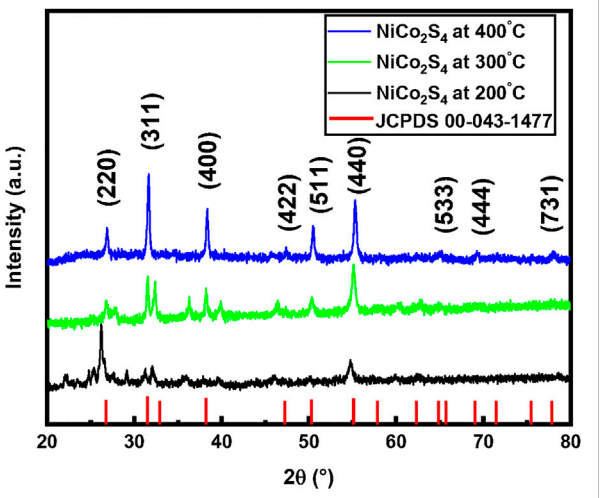

FIGURE 2
XRD spectrum of $NiCo_2S_4$ synthesized at different reaction temperatures.

Results and discussions

Different attempts have been made to obtain their optimal crystalline nanostructures at varied reaction temperatures. Figure 2 shows the XRD spectrum of $NiCo_2S_4$ nanostructures prepared at 200°C, 300°C, and 400°C respectively. The XRD spectrum obtained at 200°C does not match fully with the standard pattern of $NiCo_2S_4$, indicating that its phase is incompletely formed. Only a few peaks were matched with JCPDS card number 00-043-1477. Many extra peaks were found in the spectrum which shows the possibility of the presence of some precursor elements due to incomplete reaction. To obtain the pure crystalline phase of $NiCo_2S_4$, we further treated the ground sample at 300 °C. However, we found some extra dominant peaks in the spectrum, so still, we believe that the pure phase of $NiCo_2S_4$ at 300°C was not obtained. When we increased the reaction temperature to 400°C we get the pure crystalline phase of $NiCo_2S_4$. The observed pattern is in good agreement with the standard JCPDS card number 00-043-1477 of $NiCo_2S_4$. No extra peak was noticed in the XRD pattern, which confirmed the purity and crystallinity of the sample. The XRD analysis confirms the cubic crystal structure of $NiCo_2S_4$. Using the lattice planes and d-spacing values the lattice constants were calculated. The average lattice constants are found to be a = b = c = 9.43 Å. Our calculated values are very much closer to the standard JCPDs card and with literature results that indicate the purity of our sample. The crystallite size is calculated through Scherrer's relation. The average crystallite size of $NiCo_2S_4$ at T = 400°C is about 27 nm. We can also observe that the diffraction peaks got sharper and more dominant as the temperature was raised from 200°C to 400°C, indicating the improved crystallinity of the prepared material.

To check the preferable crystal growth direction, we calculated the texture coefficient of the prepared sample using the formula given below (Kumar et al., 2015).

$$T_c = \frac{\left(I_{hkl}/I_{r(hkl)}\right)}{\frac{1}{n}\Sigma_n\left(I_{hkl}/I_{r(hkl)}\right)} \quad (3)$$

where I_{hkl} is the intensity of the plane in the XRD spectrum of the sample, $I_{r(hkl)}$ is the intensity of the corresponding plane in the reference pattern, and "n" is the number of peaks selected for the study. Moreover, an increase in texture coefficient from 1 is said to indicate a higher degree of preferred orientation along a given plane. The texture study shows that the $NiCo_2S_4$ nanostructures are highly textured along the (533) plane.

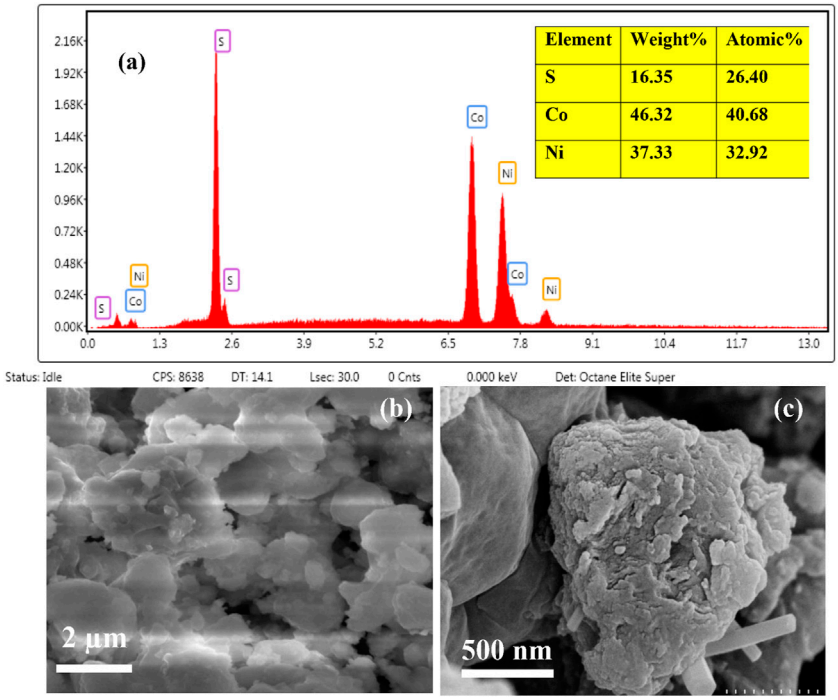

FIGURE 3
(A) EDX spectrum of $NiCo_2S_4$ **(B,C)** SEM images of $NiCo_2S_4$ at two different Resolutions.

Morphological analysis

Figure 3A shows the EDX spectrum of synthesized $NiCo_2S_4$ nanostructured. The presence of Co, Ni, and S elements and no other extra impurity peak in the graph confirms the purity of the prepared material. The detailed compositional analysis from a selected area is also shown. According to the EDX spectrum and table, the values are 26.4, 40.68, and 32.9 for S, Co, and Ni respectively. Therefore, the formula can be written as $Ni_{0.12}Co_{0.46}S_{0.12.}$ Figure 3B of the SEM image indicates that the agglomerates were assembled from randomly oriented bundles of nanoparticles adopting poly-disperse nanosheet-like morphology. Heating the acetate precursor resulted in the formation of agglomerated nanosheets of $NiCo_2S_4$. At a higher resolution in Figure 3C the agglomerates of nanostructures are more visible. Besides this agglomeration, we also see an interesting feature. Some nanorods of diameter ~92 nm emerged as shown in the figure. This transition in the morphology may be caused due to high reaction temperature during sample preparation which breaks apart the agglomerates of nanoparticles and transforms them into nanorods.

To see the more in-depth morphology of the prepared sample, TEM (Figures 4A–C) was used. We can observe poly-sized sheet-like structures in TEM images more precisely shown in red boxes. Like in SEM analysis, we also spot some nanorods stripped into the agglomerates of nanosheets as shown in Figures 4A,B. We can see some grains/crystallites and grain boundaries in Figure 4C as well. Figure 4D shows the selected area electron diffraction (SAED) pattern of $NiCo_2S_4$. The diffraction rings associated with the polycrystalline nature of the prepared material are seen in the pattern. By using the Image-J software, we have successfully calculated the corresponding d–spacing of the rings are 5.68, 3.29, 2.69, 2.06, 1.55 Å corresponding to lattice planes (111), (220), (222). (422), and (531) respectively. These calculations were very close to those values calculated from XRD analysis and JCPDS card values. Again, from the SAED pattern, the lattice parameters are calculated as a = b = c = 9.47 Å. These calculated cell parameters are in good agreement with the literature results (Mane et al., 2021).

Optical measurements

The optical analysis was studied using UV-Vis and DRS to investigate the bandgap of prepared $NiCo_2S_4$. Figure 5A shows the absorption spectrum with the inset of the Tauc plot. The absorption spectrum was recorded using the Shimadzu 1280 UV-Vis spectrophotometer. The absorption spectrum was recorded in the range of 200–800 nm at room temperature. We prepared a

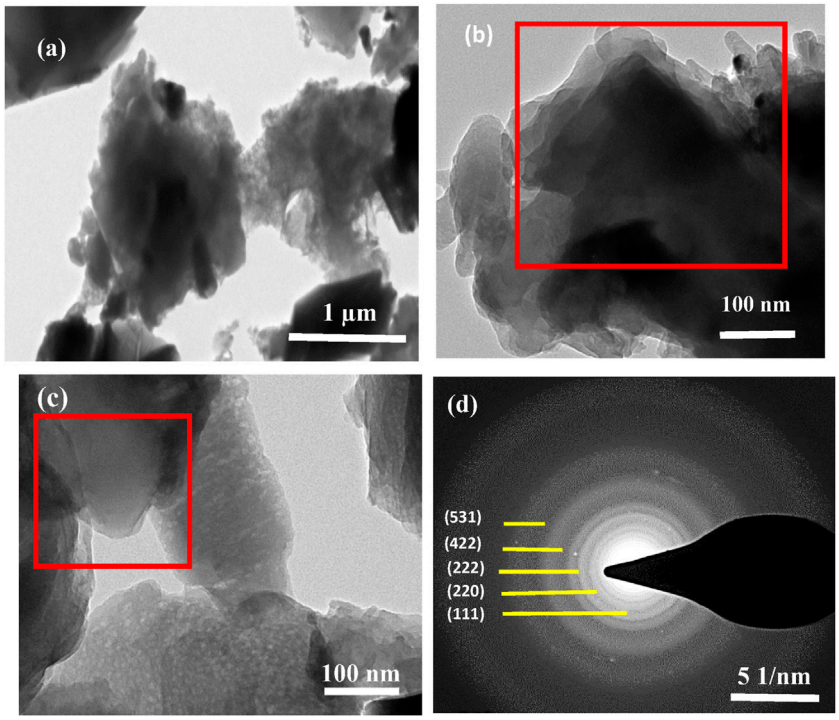

FIGURE 4
(A–C) TEM images of $NiCo_2S_4$ with different magnifications **(D)** SAED pattern of $NiCo_2S_4$.

dilute suspension of a powder sample in deionized water to check the absorbance peak. The absorption peak arises near 345 nm. The band gap of the prepared nanomaterial was calculated using the Tauc equation (Granqvist, 1995; Gnanasekar et al., 2022; Raj et al., 2022; Rajeswari et al., 2022; Rokade et al., 2022).

$$(\alpha h\nu) = A\left(h\nu - E_g\right)^n. \tag{4}$$

For the direct bandgap calculation of our specimen, a graph is plotted between $(\alpha h\nu)^2$ and photon energy $''h\nu''$ according to Beer-Lambert's law (Wagh et al., 2022). The extrapolation of a linear region to the energy axis gives us a bandgap value. The calculated bandgap of $NiCo_2S_4$ is found to be 2.03 eV as shown in the figure. This band gap value is very much close to the already reported bandgap value of this material (Sarawutanukul et al., 2020).

Further, the optical bandgap of $NiCo_2S_4$ was also investigated through DRS. Figure 5B shows the variation of percentage reflectance against the wavelength of the incident source measured in the range of 300–900 nm. While the inset of Figure 5B shows the transformed Kubelka Munk plot obtained from the reflectance data. In DRS, the absorption coefficient $''\alpha''$ is replaced by Kubelka Munk or the re-emission function which is proportional to the absorption coefficient (K) and scattering coefficient (S).

$$\frac{k}{S} = \frac{(1 - R_\infty)}{2R_\infty} \equiv F(R_\infty) \tag{5}$$

Where "R" is the measured reflected light. $NiCo_2S_4$ bandgap can be calculated by the transformed form of Eq. 4 in which $''\alpha''$ is replaced by $''F(R_\infty)''$ Kubelka Munk function (Kumar et al., 2013; Sundararajan et al., 2022a; Sundararajan et al., 2022b; Sathish Kumar et al., 2022).

$$(F(R_\infty)h\nu)^n = A\left(h\nu - E_g\right) \tag{6}$$

The "E_g" value of $NiCo_2S_4$ calculated from DRS spectroscopy is 2.17 eV as shown in the inset of Figure 5B. Again this value is very close to the bandgap value obtained from UV-Vis spectroscopy and previous literature (Zhao et al., 2020).

We also investigated the DRS spectra in more detail through the unique inverse logarithmic derivative (ILD) method (Pawlak and Al-Ani, 2019; Khan et al., 2021). By taking the natural logarithm on both sides of the Tauc Eq. 4:

$$ln(ahv) = n\,ln(A) + n\,ln\left(h\nu - E_g\right). \tag{7}$$

Here "A" is eliminated because it does not depend on the photon energy "$h\nu$" and is also less significant practically than the "n" and "E_g" factors. By differentiating Eq. 7 as a function of photon energy:

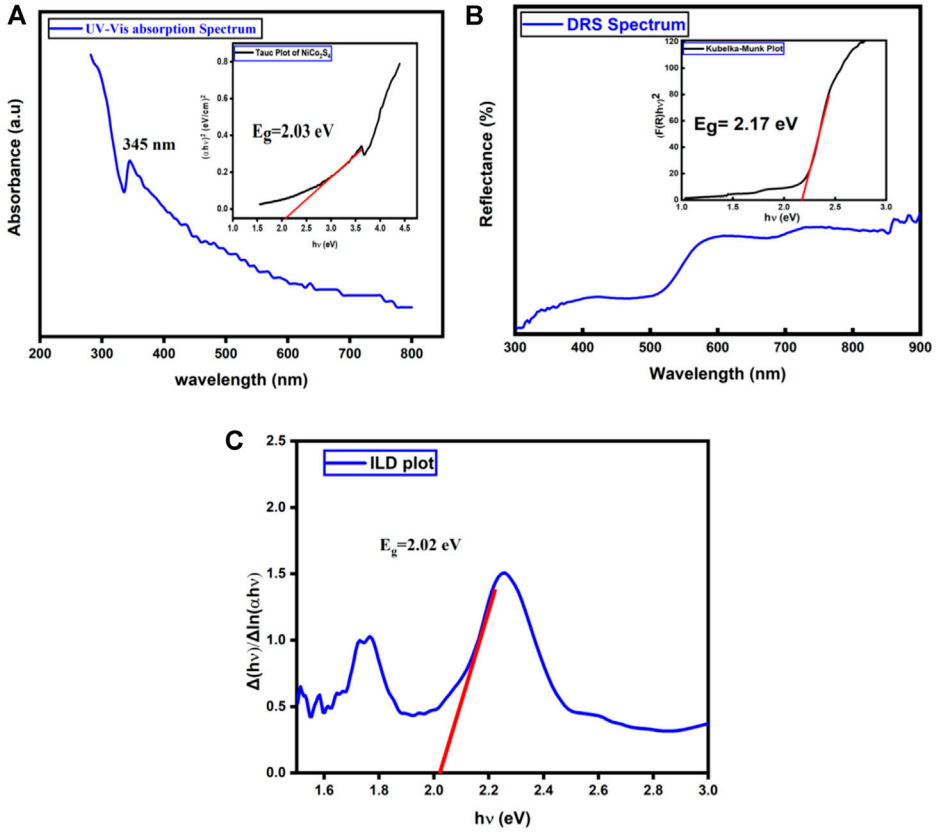

FIGURE 5
(A) Shows UV-Vis absorption spectrum and Tauc plot(inset) of $NiCo_2S_4$ nanostructures **(B)** DRS spectrum and Kubelka-Munk plot **(C)** Inverse logarithmic derivative of $\alpha h\nu$ as a function of hν (photon energy).

$$\frac{d\,ln(\alpha h\nu)}{d\,(h\nu)} = \frac{n}{h\nu - E_g}. \tag{8}$$

By inverting Eq. 8

$$\frac{d\,(h\nu)}{d\,ln(\alpha h\nu)} = \frac{h\nu - E_g}{n}. \tag{9}$$

Finally, by converting Eq. 9 into a numerical derivative:

$$\frac{\Delta\,(h\nu)}{\Delta\,ln(\alpha h\nu)} = \frac{h\nu - E_g}{n}. \tag{10}$$

Then the graph of $"\Delta\,(h\nu)/\Delta\,ln(\alpha h\nu)"$ as a function of incident photon energy is plotted which gives us the value of "E_g" by extrapolating the linear region into the energy axis. The bandgap of $NiCo_2S_4$ calculated from the "ILD" method is found to be 2.02 eV. Figure 5C shows the energy band gap graph of $NiCo_2S_4$ using the ILD method. From three different methods, the band gap value of $NiCo_2S_4$ is quite like one another and confirms the bandgap results.

As from both optical spectroscopies, $NiCo_2S_4$ has a specific optical bandgap like other semiconducting materials, therefore more detailed investigation of its metallic nature was done through temperature-dependent IV characteristics.

Electrical measurements

The temperature-dependent electrical response of the prepared material is studied using the Keithley 2401 source meter. IV characteristics of $NiCo_2S_4$ nanostructures were measured in the temperature range 300–400 K using two probe method as shown in Figure 6A. When the temperature is increased from 300 to 400 K, the current decreases, showing metallic behavior. The *ln-ln* plot of IV characteristics is drawn and shown in the inset of Figure 6A. The slope of about ~1 indicates the ohmic behavior. Figure 6B shows the zoomed part of IV characteristics. We can see clearly the decrease of conduction with the increase of temperature. The resistivity values are calculated from the IV data and are plotted against the temperature shown in Figure 6C. The increase in resistivity with temperature i.e., positive temperature coefficient of resistance indicates the metallic nature of $NiCo_2S_4$. This result

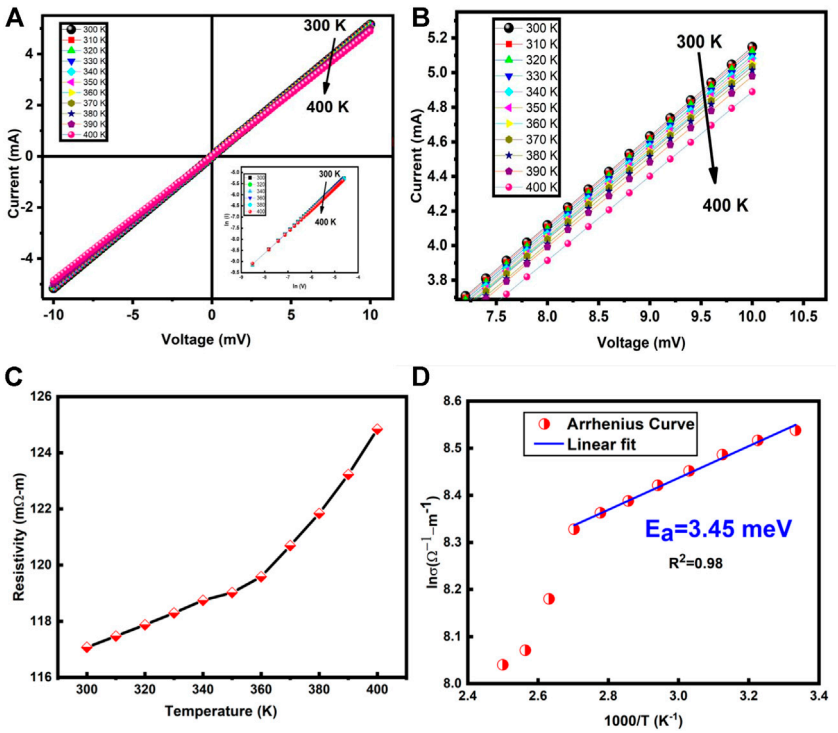

FIGURE 6
(A) IV response of $NiCo_2S_4$ at different temperatures and (inset) is the double logarithm graph of $NiCo_2S_4$ showing ohmic behavior. **(B)** Zoomed IV characteristics curves of $NiCo_2S_4$ **(C)** Resistivity varition with temperature **(D)** Arrhenius plot for the calculation of the activation energy.

TABLE 1 Comparison of the present study of $NiCo_2S_4$ with previously reported literature.

Synthesis ($NiCo_2S_4$)	Bandgap	Electrical behaviors	Morphology	References
Hydrothermal synthesis	—	Metallic behavior below the room temperature (5–300 K)	Urchin-like morphology	Xia et al. (2015)
A facile precursor transformation method	1.2 eV	Semiconducting with direct transition	Urchin-like nanostructure	Chen et al. (2013)
Solventless thermolysis synthesis	—	—	Agglomerated nanoparticles	Shombe et al. (2021)
Solvothermal process	1.71 eV with a direct bandgap transition	Prediction of metallic with no absorption in UV-Vis spectra	Quasi-spherical morphology	Du et al. (2014)
Electrodeposition method	—	—	Nanosheets Arrays	Chen et al. (2014)
Sulfurization of Ni and Co-based precursors	1.4 and 2.4 eV with a direct bandgap transition	—	3D urchin-like $NiCo_2S_4$	Sarawutanukul et al. (2020)
Solvothermal route	—	—	Mesoporous $NiCo_2S_4$ nanoparticles	Zhu et al. (2015)
Solvent-free solid-state route	2.02–2.17 eV with direct bandgap transition	Metallic nature above the room temperature (300–400 K)	Agglomerated sheet-like structures along with the growth of nanorods	Present work

of metallic behavior agreed very well with the recently reported literature (Xia et al., 2015). $NiCo_2S_4$ has a resistivity of the order of milli-ohm, making it a promising material for different energy storage and conversion applications.

Figure 6D shows the activation energy graph, plotted using the Arrhenius relation (Batool et al., 2020; Sankudevan et al., 2022) from well-fitted data in a low-temperature region. The activation energy is found to be

3.45 meV. This small value of activation energy is indicating the high cation activity (nickel and cobalt) of $NiCo_2S_4$. A comparative and detailed analysis of the literature work and our work is presented in Table 1.

Conclusion

The crystalline cubic phase of $NiCo_2S_4$ is successfully achieved using a quite simple, one-step, and inexpensive solvent-free synthesis approach. The XRD analysis confirmed the successful formation of the cubic phase of $NiCo_2S_4$. Morphological analysis through SEM and TEM shows that agglomerated sheet-like structures with unusual growth of nanorods as well were built. The bandgap of $NiCo_2S_4$ is found to be 2.02–2.17 eV through the absorption and reflectance spectrum obtained from UV-Vis and DRS spectroscopy respectively. However, the electrical measurements at 300–400 K reveal that $NiCo_2S_4$ has a positive temperature coefficient of resistance which confirms the metallic nature of $NiCo_2S_4$. The superior electrical and optical properties, the small activation energy, low resistivity at room temperature, positive temperature coefficient of resistance, and better electronic conductivity make $NiCo_2S_4$ a potential option for numerous applications in diverse domains.

Data availability statement

The raw data supporting the conclusion of this article will be made available by the authors, without undue reservation.

Author contributions

All authors listed have made a substantial, direct, and intellectual contribution to the work and approved it for publication.

Funding

(Competative research grant number 180214306).

Acknowledgments

The authors would like to thank the Higher Education Commission (HEC) of Pakistan for the financial support through NRPU projects.

Conflict of interest

The authors declare that the research was conducted in the absence of any commercial or financial relationships that could be construed as a potential conflict of interest.

Publisher's note

All claims expressed in this article are solely those of the authors and do not necessarily represent those of their affiliated organizations, or those of the publisher, the editors and the reviewers. Any product that may be evaluated in this article, or claim that may be made by its manufacturer, is not guaranteed or endorsed by the publisher.

References

Ahmad, M., Rafiq, M. A., and Hasan, M. M. (2013a). Transport characteristics and colossal dielectric response of cadmium sulfide nanoparticles. *J. Appl. Phys.* 114 (13), 133702. doi:10.1063/1.4823810

Ahmad, M., Rafiq, M. A., Imran, Z., Rasool, K., Shahid, R. N., Javed, Y., et al. (2013b). Charge conduction and relaxation in MoS_2 nanoflakes synthesized by simple solid state reaction. *J. Appl. Phys.* 114 (4), 043710. doi:10.1063/1.4816570

Ahmad, M., Rafiq, M. A., Rasool, K., Imran, Z., and Hasan, M. M. (2013c). Dielectric and transport properties of bismuth sulfide prepared by solid state reaction method. *J. Appl. Phys.* 113 (4), 043704. doi:10.1063/1.4781004

Batool, S., Imran, Z., Rasool, K., Ambreen, J., Hassan, S., Arif, S., et al. (2020). Study of electric conduction mechanisms in bismuth silicate nanofibers. *Sci. Rep.* 10 (2775), 1–10. doi:10.1038/s41598-020-59563-6

Chen, H., Jiang, J., Zhang, L., Wan, H., Qi, T., and Xia, D. (2013). Highly conductive $NiCo_2S_4$ urchin-like nanostructures for high-rate pseudocapacitors. *Nanoscale* 5 (19), 8879–8883. doi:10.1039/C3NR02958A

Chen, W., Xia, C., and Alshareef, H. N. (2014). One-step electrodeposited nickel cobalt sulfide nanosheet arrays for high-performance asymmetric supercapacitors. *ACS Nano* 8 (9), 9531–9541. doi:10.1021/nn503814y

Chia, X., Ambrosi, A., Sofer, Z., Luxa, J., and Pumera, M. (2015). Catalytic and charge transfer properties of transition metal dichalcogenides arising from electrochemical pretreatment. *ACS Nano* 9 (5), 5164–5179. doi:10.1021/acsnano.5b00501

Cui, L., Xu, H., An, Y., Xu, M., Lei, Z., and Jin, X. (2022). Electrodeposition preparation of $NiCo_2S_4$ nanoparticles on N-doped activated carbon modified graphene film for asymmetric all-solid-state supercapacitors. *New J. Chem.* 46, 12419–12426. doi:10.1039/D2NJ01729F

Du, W., Zhu, Z., Wang, Y., Liu, J., Yang, W., Qian, X., et al. (2014). One-step synthesis of $CoNi_2S_4$ nanoparticles for supercapacitor electrodes. *RSC Adv.* 4 (14), 6998–7002. doi:10.1039/c3ra46805d

Gao, Y. P., and Huang, K. J. (2017). $NiCo_2S_4$ materials for supercapacitor applications. *Chem. Asian J.* 12 (16), 1969–1984. doi:10.1002/asia.201700461

Gervas, C., Khan, M. D., Zhang, C., Zhao, C., Gupta, R. K., Carleschi, E., et al. (2018). Effect of cationic disorder on the energy generation and energy storage applications of $NixCo_{3-x}S_4$ thiospinel. *RSC Adv.* 8 (42), 24049–24058. doi:10.1039/C8RA03522A

Gnanasekar, T., Valanarasu, S., Ubaidullah, M., Alam, M., Nafady, A., Mohanraj, P., et al. (2022). Fabrication of Er, Tb doped CuO thin films using nebulizer spray pyrolysis technique for photosensing applications. *Opt. Mater.* 123, 111954. doi:10.1016/j.optmat.2021.111954

Granqvist, C. G. (1995) *Handbook of inorganic electrochromic materials*. Elsevier.

Guan, B. Y., Yu, L., Wang, X., Song, S., and Lou, X. W. (2017) *Form. onion like $NiCo_2S_4$ Part. via sequentialion Exch. hybrid supercapacitors. Adv. Mat.* 29 (6): 1605051. doi:10.1002/adma.201605051

Hu, L., Wu, L., Liao, M., Hu, X., and Fang, X. (2012). Electrical transport properties of large, individual $NiCo_2O_4$ nanoplates. *Adv. Funct. Mat.* 22 (5), 998–1004. doi:10.1002/adfm.201102155

Khan, M. D., Murtaza, G., Revaprasadu, N., and O'Brien, P. (2018). Synthesis of chalcopyrite-type and thiospinel minerals/materials by low temperature melts of xanthates. *Dalton Trans.* 47 (27), 8870–8873. doi:10.1039/C8DT00953H

Khan, S., Hussain, A., He, K., Liu, B., Imran, Z., Ambreen, J., et al. (2021). Tailoring the bandgap of Mn_3O_4 for visible light driven photocatalysis. *J. Environ. Manag.* 293, 112854. doi:10.1016/j.jenvman.2021.112854

Kumar, S. S., Rubio, E., Noor-A-Alam, M., Martinez, G., Manandhar, S., Shutthanandan, V., et al. (2013). Structure, morphology, and optical properties of amorphous and nanocrystalline gallium oxide thin films. *J. Phys. Chem. C* 117 (8), 4194–4200. doi:10.1021/jp311300e

Kumar, M., Kumar, A., and Abhyankar, A. (2015). Influence of texture coefficient on surface morphology and sensing properties of w-doped nanocrystalline tin oxide thin films. *ACS Appl. Mat. Interfaces* 7 (6), 3571–3580. doi:10.1021/am507397z

Lin, J-Y., and Chou, S-W. (2013). Highly transparent $NiCo_2S_4$ thin film as an effective catalyst toward triiodide reduction in dye-sensitized solar cells. *Electrochem. Commun.* 37, 11–14. doi:10.1016/j.elecom.2013.09.027

Mane, S. M., Pawar, S. S., Go, J. S., Teli, A. M., and Shin, J. C. (2021). Asymmetric supercapacitor properties of fern-like nanostructured $NiCo_2S_4$ synthesized through a one-pot simple solvothermal method. *Mater. Lett.* 301, 130262. doi:10.1016/j.matlet.2021.130262

Nan, H., Han, J., Luo, Q., Yin, X., Zhou, Y., Yao, Z., et al. (2018). Economically synthesized $NiCo_2S_4$/reduced graphene oxide composite as efficient counter electrode in dye-sensitized solar cell. *Appl. Surf. Sci.* 437, 227–232. doi:10.1016/j.apsusc.2017.12.175

Patil, A. D., Patange, S. M., Dighe, P. M., Shaikh, S. F., Rana, AuH. S., Pandit, B., et al. (2022). Tuning the structural, optical and magnetic properties of NiCuZn ($Ni_{0.4}Cu_{0.3}Zn_{0.3}Fe_2O_4$) spinel ferrites by Nb_2O_5 additive. *Ceram. Int.* 48 (18), 27039–27050. doi:10.1016/j.ceramint.2022.06.016

Pawlak, J., and Al-Ani, S. (2019). Inverse logarithmic derivative method for determining the energy gap and the type of electron transitions as an alternative to the Tauc method. *Opt. Mater.* 88, 667–673. doi:10.1016/j.optmat.2018.12.041

Raj, I. L. P., Valanarasu, S., Vinoth, S., Chidhambaram, N., Isaac, R. S. R., Ubaidullah, M., et al. (2022). Highly sensitive ultraviolet photodetectors fabricated from rare Earth metal ions doped NiO thin films via nebulizer spray pyrolysis method. *Sensors Actuators A Phys.* 333, 113242. doi:10.1016/j.sna.2021.113242

Rajeswari, S., Ibrahim, M. M., Al-Enizi, A. M., Ubaidullah, M., Arunachalam, P., Pandit, B., et al. (2022). Photo-sensing properties of Cd-doped In_2S_3 thin films fabricated via low-cost nebulizer spray pyrolysis technique. *J. Mat. Sci. Mat. Electron.* 33 (24), 19284–19296. doi:10.1007/s10854-022-08766-w

Rokade, A., Jadhav Â, Y., Jathar Â, S., Rahane Â, S., Barma Â, S., Rahane Â, G., et al. (2021). it i, Pawar Â J, Roy Â A, Â S Â, Jadkar e (2022) Realization of Electrochemically Grown a-Fe_2O_3 Thin Films for Photoelectrochemical Water Splitting Application. *Eng. Sci.* 17, 242–255. doi:10.30919/es8d532

Sankudevan, P., Sakthivel, R. V., Prakasam, A., Al-Enizi, A. M., Ubaidullah, M., Pandit, B., et al. (2022). Enhancement of luminescence mechanisms in structural, morphological, and catalytic properties of undoped $CuCr_2O_4$ and Mn-doped $CuCr_2O_4$. *J. Clust. Sci.* 70, doi:10.1007/s10876-022-02328-0

Sarawutanukul, S., Tomon, C., Duangdangchote, S., Phattharasupakun, N., and Sawangphruk, M. (2020). Rechargeable photoactive Zn-air batteries using $NiCo_2S_4$ as an efficient bifunctional photocatalyst towards OER/ORR at the cathode. *Batter. Supercaps* 3 (6), 541–547. doi:10.1002/batt.201900205

Sathish Kumar, S., Valanarasu, S., Gunavathy, K. V., Vinoth, S., Haunsbhavi, K., Alagarasan, D., et al. (2022). Enhancing the photodetection property of CdSe thin films via thermal evaporation technique: Role of substrate temperature. *Phys. Scr.* 97 (5), 055807. doi:10.1088/1402-4896/ac619c

Shombe, G. B., Razzaque, S., Khan, M. D., Nyokong, T., Mashazi, P., Choi, J., et al. (2021). Low temperature scalable synthetic approach enabling high bifunctional electrocatalytic performance of $NiCo_2S_4$ and $CuCo_2S_4$ thiospinels. *RSC Adv.* 11 (50), 31533–31546. doi:10.1039/D1RA02309H

Shombe, G. B., Khan, M. D., Choi, J., Gupta, R. K., Opallo, M., and Revaprasadu, N. (2022). Tuning composition of $CuCo_2S_4$–$NiCo_2S_4$ solid solutions via solvent-less pyrolysis of molecular precursors for efficient supercapacitance and water splitting. *RSC Adv.* 12 (17), 10675–10685. doi:10.1039/D2RA00815G

Sundararajan, M., Bonisha, B., Ubaidullah, M., Shaikh, S. M. F., Revathi, S., Thiripurasundari, D., et al. (2022a). Enhanced visible light photocatalytic degradation of rhodamine B using $Ni_{1-x}Ca_xFe_2O_4$ ($0 \le x \le 0.5$) nanoparticles: Performance, kinetics and mechanism. *Mater. Res. Bull.* 154, 111911. doi:10.1016/j.materresbull.2022.111911

Sundararajan, M., Subramani, A., Ubaidullah, M., Shaikh, S. F., Pandit, B., Jesudoss, S. K., et al. (2022b). Synthesis, characterization and *in vitro* cytotoxic effects of Cu:Co_3O_4 nanoparticles via microwave combustion method. *J. Clust. Sci.* 33 (4), 1821–1830. doi:10.1007/s10876-022-02239-0

Tong, Y., Yu, X., Wang, H., Yao, B., Li, C., and Shi, G. (2018). Trace level Co–N doped graphite foams as high-performance self-standing electrocatalytic electrodes for hydrogen and oxygen evolution. *ACS Catal.* 8 (5), 4637–4644. doi:10.1021/acscatal.8b01131

Wagh, S. S., Jagtap, C. V., Kadam, V. S., Shaikh, S. F., Ubaidullah, M., Pandit, B., et al. (2022). Silver doped ZnO nanoparticles synthesized for photocatalysis application. *ES Energy Environ.* 17, 94–105. doi:10.30919/esee8e720

Wang, S., Li, W., Xin, L., Wu, M., and Lou, X. (2016). High-performance nickel cobalt sulfide materials via low-cost preparation for advanced asymmetric supercapacitors. *RSC Adv.* 6 (48), 42633–42642. doi:10.1039/C6RA04462J

Wang, P., Li, C., Dong, S., Ge, X., Zhang, P., Miao, X., et al. (2019). Hierarchical $NiCo_2S_4$@ NiO core–shell heterostructures as catalytic cathode for long-life Li-O_2 batteries. *Adv. Energy Mat.* 9 (24), 1900788. doi:10.1002/aenm.201900788

Wei, C., Huang, Y., Xue, S., Zhang, X., Chen, X., Yan, J., et al. (2017). One-step hydrothermal synthesis of flaky attached hollow-sphere structure $NiCo_2S_4$ for electrochemical capacitor application. *Chem. Eng. J.* 317, 873–881. doi:10.1016/j.cej.2017.02.130

Wu, Y., Liu, X., Han, D., Song, X., Shi, L., Song, Y., et al. (2018). Electron density modulation of $NiCo_2S_4$ nanowires by nitrogen incorporation for highly efficient hydrogen evolution catalysis. *Nat. Commun.* 9 (1), 1425–1429. doi:10.1038/s41467-018-03858-w

Xia, C., Li, P., Gandi, A. N., Schwingenschlögl, U., and Alshareef, H. N. (2015). Is $NiCo_2S_4$ really a semiconductor? *Chem. Mat.* 27 (19), 6482–6485. doi:10.1021/acs.chemmater.5b01843

Xin, C., Ang, L., Musharavati, F., Jaber, F., Hui, L., Zalnezhad, E., et al. (2020). Supercapacitor performance of nickel-cobalt sulfide nanotubes decorated using Ni Co-layered double hydroxide nanosheets grown *in situ* on Ni foam. *Nanomaterials* 10 (3), 584. doi:10.3390/nano10030584

Yang, J., Bao, C., Zhu, K., Yu, T., Li, F., Liu, J., et al. (2014). High catalytic activity and stability of nickel sulfide and cobalt sulfide hierarchical nanospheres on the counter electrodes for dye-sensitized solar cells. *Chem. Commun.* 50 (37), 4824–4826. doi:10.1039/C4CC00001C

Yu, J-F., and Lin, L-Y. (2016). Structure variation of nickel cobalt sulfides using Ni foam and nickel salt as the nickel source and the application on the supercapacitor electrode. *J. Energy Storage* 7, 295–304. doi:10.1016/j.est.2016.08.004

Zhang, Z., Wang, X., Cui, G., Zhang, A., Zhou, X., Xu, H., et al. (2014). $NiCo_2S_4$ sub-micron spheres: An efficient non-precious metal bifunctional electrocatalyst. *Nanoscale* 6 (7), 3540–3544. doi:10.1039/C3NR05885A

Zhao, S., Xu, J., Liu, Z., and Li, Y. (2020). Graphene quantum dots synthesized by green method regulate electron transport on the surface of hollow spherical $NiCo_2S_4$ for efficient photocatalytic H_2 evolution. *J. Solid State Chem.* 288, 121428. doi:10.1016/j.jssc.2020.121428

Zheng, Y., Xu, J., Yang, X., Zhang, Y., Shang, Y., and Hu, X. (2018). Decoration $NiCo_2S_4$ nanoflakes onto Ppy nanotubes as core-shell heterostructure material for high-performance asymmetric supercapacitor. *Chem. Eng. J.* 333, 111–121. doi:10.1016/j.cej.2017.09.155

Zhu, Y., Wu, Z., Jing, M., Yang, X., Song, W., and Ji, X. (2015). Mesoporous $NiCo_2S_4$ nanoparticles as high-performance electrode materials for supercapacitors. *J. Power Sources* 273, 584–590. doi:10.1016/j.jpowsour.2014.09.144